Long-term monitoring of transplanted human neural stem cells in developmental and pathological contexts with MRI

Raphael Guzman*, Nobuko Uchida†, Tonya M. Bliss*, Dongping He†, Karen K. Christopherson†, David Stellwagen‡, Alexandra Capela‡, Joan Greve§, Robert C. Malenka‡, Michael E. Moseley§, Theo D. Palmer*, and Gary K. Steinberg*¶

*Department of Neurosurgery, Stanford University School of Medicine, 300 Pasteur Drive, R200, Stanford, CA 94305-5327; †StemCells, Inc., 3155 Porter Drive, Palo Alto, CA 94304-1213, ‡Department of Psychiatry and Behavioral Sciences, Stanford University School of Medicine, MSLS P104, Stanford, CA 94305-5485; and §Department of Radiology, Lucas Magnetic Resonance Spectroscopy and Imaging Center, Stanford University School of Medicine, P286, Stanford, CA 94022

Edited by Irving L. Weissman, Stanford University School of Medicine, Stanford, CA, and approved April 24, 2007 (received for review October 6, 2006)

Noninvasive monitoring of stem cells, using high-resolution molecular imaging, will be instrumental to improve clinical neural transplantation strategies. We show that labeling of human central nervous system stem cells grown as neurospheres with magnetic nanoparticles does not adversely affect survival, migration, and differentiation or alter neuronal electrophysiological characteristics. Using MRI, we show that human central nervous system stem cells transplanted either to the neonatal, the adult, or the injured rodent brain respond to cues characteristic for the ambient microenvironment resulting in distinct migration patterns. Nanoparticle-labeled human central nervous system stem cells survive long-term and differentiate in a site-specific manner identical to that seen for transplants of unlabeled cells. We also demonstrate the impact of graft location on cell migration and describe magnetic resonance characteristics of graft cell death and subsequent clearance. Knowledge of migration patterns and implementation of noninvasive stem cell tracking might help to improve the design of future clinical neural stem cell transplantation.

superparamagnetic iron oxide | stem cell biology

Advances in neural transplantation have paved the way for clinical trials aimed at restoring brain function in diseases, such as Parkinson's (1–3) and Huntington's (4), and stroke (5). The success of these trials for neurological diseases will depend not only on patient selection criteria and on choosing the right cell type, but also on the timing and site of transplantation. Both variables can influence the transplanted stem cells' migration pattern and subsequent differentiation (6, 7). Therefore, long-term monitoring of the graft in relation to the evolving lesion will be crucial.

MRI, with its high spatial resolution, is the ideal modality for *in vivo* cell tracking. Tagging cells with superparamagnetic iron oxide (SPIO) nanocomposites has been shown to induce sufficient MR cell contrast for *in vivo* imaging of neural cell migration (8, 9). Previous studies have demonstrated its application to track stem cells after stroke, but these were done with non-human stem cells and lacked in-depth analysis of the SPIO effect on stem cell biology (10, 11).

Before this method can be considered to label human neural stem cells for clinical application, further analysis of the effects of SPIO on the biology of human stem cells are needed. For example, it has been described that Feridex, a SPIO reagent approved by the United States Food and Drug Administration for human use, inhibits mesenchymal stem cells from differentiating into chondrocytes (12), emphasizing the need for in-depth analysis of the influence of magnetic labeling on stem cell biology.

We investigated the effects of SPIO labeling on human central nervous system stem cells grown as neurospheres (hCNS-SCns) (6, 13–15) *in vitro* and *in vivo*. We show that SPIO-labeled hCNS-SCns proliferate and differentiate normally *in vitro* and exhibit neuronal electrophysiological characteristics. We then used MRI to analyze migration patterns of SPIO-labeled hCNS-SCns transplanted into newborn and adult (injured and uninjured) rodent brain. We find that SPIO-labeled hCNS-SCns exhibit a similar extent of survival, migration, integration, and differentiation after transplantation into the rodent brain as their unlabeled counterparts.

Results

***In vitro* Characterization and MRI of SPIO-Labeled Human Neural Stem Cells.** We first demonstrate that labeling of human neural stem cells is feasible and does not impair cell viability and biological characteristics *in vitro*. HCNS-SCns were labeled with Feridex and protamine sulfate and tested for labeling efficiency, cell proliferation, differentiation as well as electrophysiological behavior. SPIO was detected in the cytoplasm (Fig. 1*A*). We achieved a 98% labeling efficiency as determined by Prussian Blue staining [supporting information (SI) Fig. 5]. Cell viability for SPIO-labeled and unlabeled hCNS-SCns was 92 ± 3% vs. 96 ± 2%, respectively. There was no difference in the proliferation rate between SPIO-labeled and unlabeled hCNS-SCns (Fig. 1*B*).

We analyzed the effect of cell proliferation on iron concentration. SPIO-labeled hCNS-SCns were grown under proliferative conditions for 9 days, cell samples were stained with an anti-dextran antibody and the relative iron content per cell measured. On average, the SPIO content per cell was halved every 3 days in culture, which correlated with cell doubling time (Fig. 1*C* and SI Fig. 5).

We compared the differentiation potential of SPIO-labeled and unlabeled hCNS-SCns *in vitro*. After 10 days under differentiation conditions, an average of 35.5% (± 4) of the cells were Nestin-positive, 56.2% (± 7.7) were β-tubulin-positive, and 19.4% (± 3.5) were glial fibrillary acidic protein (GFAP)-positive (Fig. 1*D*) in the SPIO-labeled hCNS-SCns. There was no statistically significant difference between the two groups (Fig. 1*D*).

Whole-cell patch-clamp recordings were made from SPIO-labeled and unlabeled hCNS-SCns 28 days after differentiation. Cells displaying a typical neuronal morphology (two to five well defined primary processes (16) were chosen for the recordings.

Author contributions: R.G., R.C.M., M.E.M., T.D.P., and G.K.S. designed research; R.G., T.M.B., K.K.C., D.S., and J.G. performed research; N.U., D.H., K.K.C., and A.C. contributed new reagents/analytic tools; R.G., T.M.B., D.S., J.G., R.C.M., and M.E.M. analyzed data; and R.G., T.D.P., and G.K.S. wrote the paper.

Conflict of interest statement: N.U., D.H., K.K.C., and A.C. are employees of StemCells, Inc. I.W. is on the Scientific Advisory Board of StemCells, Inc. StemCells, Inc. provided the human neural stem cells and human-specific antibodies.

This article is a PNAS Direct Submission.

Abbreviations: GFAP, glial fibrillary acidic protein; hCNS-SCns, human central nervous system stem cells grown as neurospheres; OB, olfactory bulb; RMS, rostral migratory stream; SPIO, superparamagnetic iron oxide; SVZ, subventricular zone.

¶To whom correspondence should be addressed. E-mail: gsteinberg@stanford.edu.

This article contains supporting information online at www.pnas.org/cgi/content/full/0608519104/DC1.

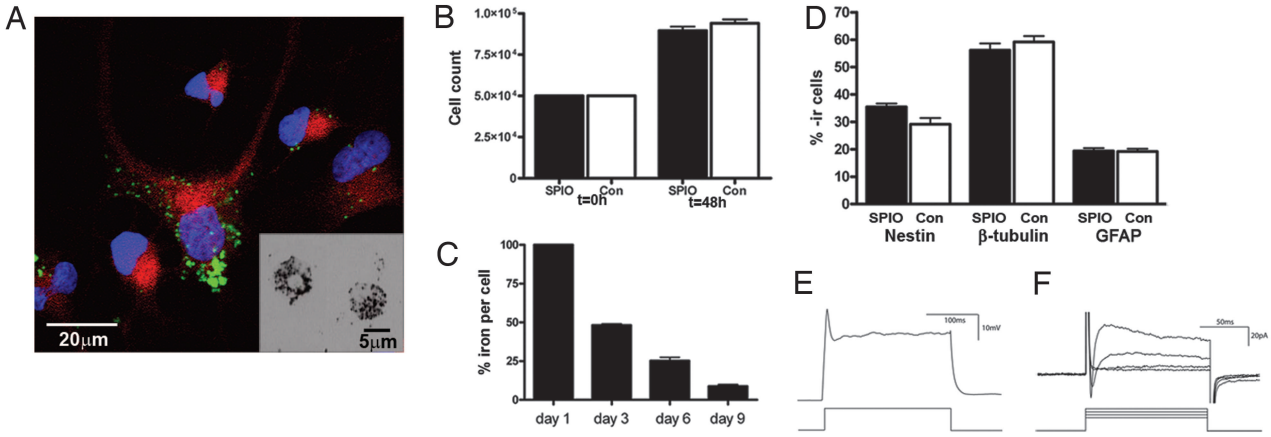

Fig. 1. *In vitro* analysis of SPIO-labeled hCNS-SCns. SPIO labeling was efficient and did not affect proliferation, differentiation and electrophysiology of hCNS-SCns *in vitro*. (*A*) hCNS-SCns stained with an anti-dextran antibody (DX-1 in green) and a human-specific cytoplasmic marker (SC121, red; DAPI, blue) 6 days after *in vitro* proliferation. (*Inset*) hCNS-SCns stained for DX-1 for quantitative analysis of iron content. (*B*) Proliferation of SPIO-labeled (filled bars) and unlabeled hCNS-SCns (open bars) analyzed 48 h after labeling. (*C*) The SPIO content is reduced by 50% with each division over 9 days. (*D*) Analysis of labeled and unlabeled hCNS-SCns grown under differentiation conditions for 10 days revealed no difference in cell fate. Results are means ± SEM. (*E–F*) Electrophysiological cell properties were not changed after SPIO labeling of hCNS-SCns. (*E*) Action potential in a neural progenitor cells-derived neuron recorded in response to a current injection of 80 pA. (*F*) Voltage-activated sodium and potassium currents in a neural progenitor cells-derived neuron, steps of 35–65 mV.

Injection of a depolarizing current triggered indistinguishable single action potentials in cells from both groups (Fig. 1*E*), and voltage-gated Na^+ and K^+ currents were evoked from stem cell-derived neurons in both groups (Fig. 1*F*). Expression of β-III tubulin and the neuronal somatodendritic protein MAP2 was used to confirm the neuronal identity of the measured cell populations.

We also found that the graft size of 5×10^4 SPIO-labeled cells measured by *in vivo* MRI was similar to the graft size measured on a representative histological section. Moreover, the size of the signal change seen on T2-weighted imaging caused by 5×10^4 SPIO-labeled cells in an agarose gel was comparable with the signal change of the same number of labeled cells transplanted to the rat brain (SI Fig. 6).

SPIO-Labeled Human Neural Stem Cells Undergo Widespread Migration Along Natural Tracts in the Neonatal NOD-SCID Brain and Differentiate into Neurons and Glia. We and others have shown that the immature neonatal brain represents a unique environment to test the natural migration, integration, and differentiation of transplanted progenitor cells (14, 17). In the olfactory system of rodents, the progeny of endogenous stem cells that have proliferated in the subventricular zone (SVZ) enter the rostral migratory stream (RMS) and migrate to the olfactory bulb, where they integrate in a site-specific manner (14).

We asked whether MRI could be used to follow the natural migration of SPIO-labeled hCNS-SCns and whether SPIO labeling impairs migration and differentiation of hCNS-SCns *in vivo*. Immediately after transplantation, distribution of hCNS-SCns in the ventricular system could be seen by MRI. Three weeks after transplantation, hCNS-SCns were distributed in the lateral and fourth ventricle (Fig. 2*A*). Cells migrating along the RMS were detected as a bilateral hypointense area on T2-weighted spin echo and 3D gradient-echo MRI (Fig. 2*A*; gradient-echo images are shown in SI Fig. 7). On subsequent MRI at 9 and 12 weeks (data not shown), we detected migration from the SVZ into the corpus callosum, extending posteriorly into the hippocampus and cortex and anteriorly into the RMS and olfactory glomerulus. This migration remained visible up to 18 weeks (Fig. 2*B*). Migration, integration, and differentiation were subsequently studied on sagittal sections stained for the human-specific marker SC121. In agreement with MRI, SC121 staining showed human cells in the lateral ventricle integrating into the SVZ and migrating along the RMS (Fig. 2*D*). Over 18 weeks, we found progressively more widespread integration of hCNS-SCns into the host brain with site-specific integration into the SVZ, the hippocampus, the cortex and the olfactory bulb (OB) (Fig. 2 *E* and *F*). Microscopic images at higher magnification clearly demonstrate integration into the hippocampus along CA1, CA3, and the dentate gyrus (Fig. 2*G*). In the olfactory bulb, hCNS-SCns adopt laminar positions (Fig. 2*H*). Cell counting using unbiased stereology revealed no statistically significant differences in the distribution and number of surviving SPIO-labeled and unlabeled hCNS-SCns (Fig. 2*I*). To demonstrate the histological correlate to the MRI signal changes, adjacent sections were stained with Prussian blue and the human-specific marker SC121. At 3 weeks, we found distinct punctuate Prussian blue staining in the olfactory bulb, a site to which many SC121-positive human cells had migrated (SI Fig. 8 *A–C*). To prove double labeling, two adjacent paraffin sections were stained with Prussian blue or the human-specific marker SC121. The sections were superimposed, and cells were found with overlapping Prussian blue and SC121 staining (SI Fig. 8 *D–F*). Double immunohistochemistry with the panmonocytic marker Iba-1 and SC121 did not reveal double-labeled cells in the migrating cell population in the RMS, making it unlikely that the observed migration was mainly caused by SPIO-laden macrophages (SI Fig. 8 *G* and *H*).

To quantify cell fate at 18 weeks, double immunofluorescence stainings were done by using human-specific and neuronal-specific antibodies (SI Fig. 9 *A–C*). A human-specific anti-GFAP antibody was used to quantify astroglial differentiation (SI Fig. 9*D*). Overall, there was no statistically significant difference between SPIO-labeled and unlabeled hCNS-SCns (Fig. 2 *J* and *K*). In the SVZ, 9.3% (±1.3) of the cells were positive for both β-III tubulin and SC101. In the RMS, 9.4% (±1.6) cells were double-positive. Few hCNS-SCns in the SVZ and RMS expressed GFAP (5.5% ± 1.3). Migrating hCNS-SCns in the RMS also expressed doublecortin. At 18 weeks, 19.6% of the hCNS-SCns were in the OB. Of these, 17% (±4.5) expressed β-III tubulin and numerous cells were double-labeled for both MAP-2 and SC121. There was no GFAP expression in the OB.

We asked whether SPIO-labeled hCNS-SCns would elicit a more pronounced inflammatory response than unlabeled hCNS-SCns. We found no difference in Iba-1 reactivity, a panmonocytic marker, between SPIO-labeled grafts and unlabeled grafts at 18 weeks after

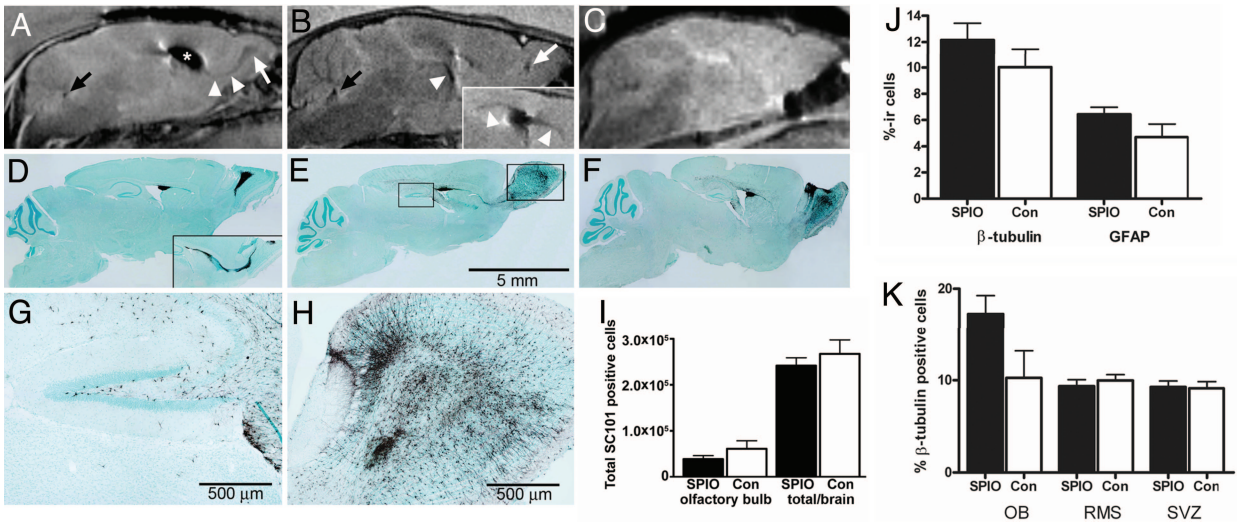

Fig. 2. Migration and integration of SPIO-labeled hCNS-SCns. MRI detects widespread migration of SPIO-labeled hCNS-SCns after intraventricular injection in the P0/P1 NOD-SCID mouse brain. (*A* and *D*) (*A*) Three weeks after transplantation, sagittal MRI shows hypointensities representing SPIO-labeled hCNS-SCns in the lateral ventricle (asterisk), along the RMS, (arrowheads) toward the OB (arrow) and in the 4th ventricle (black arrow). (*D*) corresponding section stained with the human-specific cytoplasmic marker SC121. (Inset) Shows RMS in adjacent section. (*B* and *E*) (*B*) sagittal MRI 18 weeks after transplantation showing that hCNS-SCns have integrated in the ventricular wall (arrowhead), in the core of the OB (white arrow) and in the fourth ventricle (black arrow). (*Insert*) Demonstrates migration along the corpus callosum (arrowheads). (*E*) Corresponding histological section. (*C* and *F*) (*C*) sagittal MRI of a control animal transplanted with unlabeled hCNS-SCns 18 weeks after transplantation shows no cell signal. (*F*) Corresponding histological section. (*G–H*) Higher magnification sagittal images (areas boxed in Fig. 2*E*) show hCNS-SCns in the CA1, CA3, and dentate gyrus of the hippocampus (*G*) and in the OB (*H*) of the NOD-SCID mouse. (*I*) There was a robust cell survival at 18 weeks after transplantation without statistically significant difference between SPIO-labeled ($n = 4$ animals) and unlabeled cells ($n = 3$ animals). Results are mean ± SEM. (*J* and *K*) Quantification of SC101-positive human cells coexpressing β-tubulin or GFAP overall (*J*) and coexpressing β-tubulin in anatomical subregions in NOD-SCID mice 18 weeks after intraventricular transplantation of hCNS-SCns (*K*). There was no statistically significant difference between SPIO-labeled and -unlabeled cells in terms of cell fate. OB, olfactory bulb; RMS, rostral migratory stream; SVZ, subventricular zone. Results are mean ± SEM.

transplantation (data not shown). Based on cell morphology, most of the Iba-1-positive cells were considered resting microglia.

Stroke Induces Targeted Migration of SPIO-Labeled Human Neural Stem Cells in the Adult Rat Brain. Using a stroke and transplantation paradigm (6), we show a targeted intraparenchymal migration of hCNS-SCns *in vivo*, whereas no migration was observed in the uninjured rodent brain. Seven days after a distal middle cerebral artery occlusion, rats received three cortical grafts of 1×10^5 hCNS-SCns each, medial to the cortical stroke. MRI 1 day before transplantation ruled out signal changes that could have been similar to the signal of transplanted hCNS-SCns. SPIO-labeled hCNS-SCns were detected as strongly hypointense areas in the cortex medial to the cortical stroke on T2-weighted images at 1 week (Fig. 3*A*). At 5 weeks, transparenchymal-targeted migration was clearly detected on MRI extending from the lateral graft edge toward the injured brain (Fig. 3*C*). This was confirmed histologically (Fig. 3*F*). The extent of cellular migration observed *in vivo* with MRI was visualized by using 3D reconstructions with surface rendering (Fig. 3 *B*, *D*, and *E* and SI Movies 1 and 2).

We tested the influence of the distance between the graft and the ischemic brain tissue on targeted stem cell migration by transplanting hCNS-SCns in stroked rats adjacent to the lesion border or adjacent to the midline (far from the ischemic brain tissue) with and without connection to corpus callosum. We found that in animals where hCNS-SCns were transplanted far from the lesion there was no transparenchymal cell migration (SI Fig. 10 *A–C*). In cases where the bolus of stem cells was in continuity with the corpus callosum, the stem cells underwent transcallosal migration despite greater distance to the lesion edge (SI Fig. 10 *D–F*). Transcallosal migration has been shown for stem cells transplanted in the hemisphere contralateral to the stroke (10, 18). If transplantation was adjacent to the lesion, we observed transparenchymal-targeted migration as shown in Fig. 3. In animals displaying a targeted cell migration the mean graft to lesion distance was 0.81 mm, whereas it was 3.48 mm in animals without migration (SI Fig. 10*G*).

Total surviving hCNS-SCns in immunosuppressed stroked rats 5 weeks after transplantation was 51.3% (38.9–74.6%). This compared favorably with the data in ref. 6, using the same cells and the same lesion and same transplantation paradigm where we found 33.4% cell survival.

MRI Detects Clearance of Dead Human Neural Stem Cells. MRI detection of graft rejection or death and clearance of the transplanted cells will be a critical aspect in the application of MRI for future clinical studies. SPIO-labeled hCNS-SCns were killed by repeated freeze–thaw cycles before transplantation into the left striatum of immunosuppressed Sprague–Dawley rats. Viable cells were transplanted on the contralateral side. Imaging 2 days after transplantation showed bilateral hypointense areas, representing the grafts (Fig. 4*A*). Whereas only minimal signal changes over 35 days were observed on the side with viable cells, there was a marked reduction in signal strength and graft volume on the side with dead cells (Fig. 4 *B* and *C*). The initial graft volume as measured on MRI was 1.64 mm^3 and dropped by 52% over the 35 days of observation (Fig. 4*G*). Fluorescence microscopy on sections stained for Iba-1 and the human-specific cytoplasmic marker SC121 demonstrated significantly more activated Iba-1-positive cells in rats with dead grafts as compared with rats with viable grafts (Fig. 4 *D–F*).

Discussion

Tracking cells *in vivo* has traditionally been performed by using extensive longitudinal studies where animals are killed at multiple time points. This can be circumvented by using noninvasive methods for tracking cells in real time. Several papers have explored the feasibility of tracking stem cells transplanted to the injured brain and spinal cord (19, 20), including studies in stroke (10, 11, 21). Although the ability to track various types of tagged stem cells by

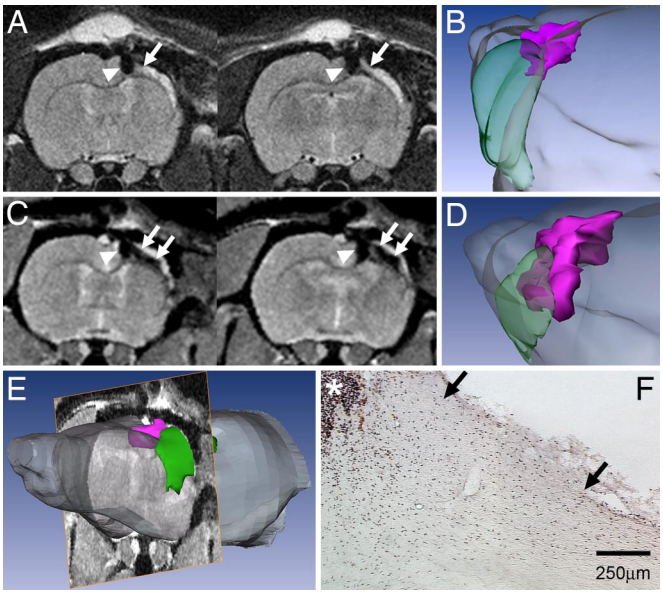

Fig. 3. Migration in the stroked brain, 3D graft morphology, and graft location. MRI detects intraparenchymal-targeted migration of hCNS-SCns toward the ischemic brain. (*A–F*) Rats were transplanted 7 days after distal middle cerebral artery occlusion, with 3×10^5 cells in three deposits. (*A* and *C*) two consecutive coronal sections showing the bolus of hCNS-SCns (arrowhead) medial to the hyperintense stroke area in T2-weighted images 1 week (*A*) and 5 weeks (*C*) after transplantation. There is some callosal (arrow) but no intraparenchymal migration at 1 week (*A*). At 5 weeks after transplantation, robust migration of hCNS-SCns toward the lesion is visible as a hypointense area on the edge of the bolus extending laterally (arrows) (*C*). Three-dimensional reconstruction and surface rendering of the rat brain based on high resolution T2-MRI as illustrated in (*E*). Posterior view of the rat brain 1 (*B*) and 5 (*D*) weeks after transplantation showing the graft (pink) and the stroked area (green). Note the broad migration of hCNS-SCns along the medial border of the stroke in the anterior posterior and craniocaudal direction, resulting in a significant increase in graft volume. (*E*) Three-dimensional reconstruction of the rat brain illustrating the segmentation process of the stroked area (green) and the graft (pink) based on coronal T2-MRI. (*F*) Histological section corresponding to the MRI (*C*) at 5 weeks stained with the human-specific nuclear marker SC101, showing the lateral bolus edge on the left side (asterisk) and robust migration (arrows) toward the infarct.

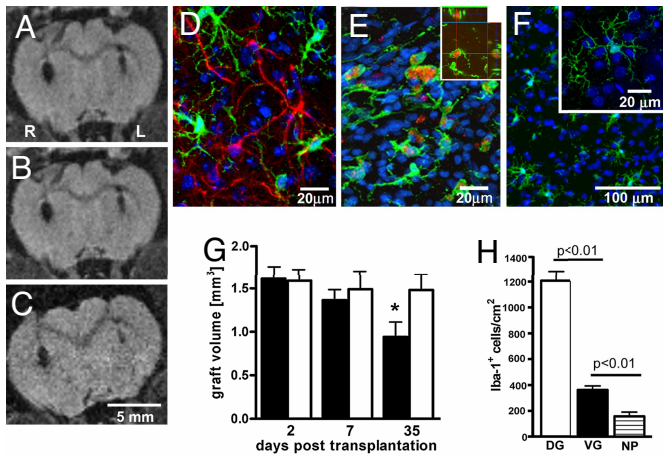

Fig. 4. Graft undergoing necrosis. Immunosuppressed rats were transplanted with viable hCNS-SCns into the right striatum and dead hCNS-SCns (three freeze–thaw passages) into the left striatum. Early loss of MR signal and graft volume indicates graft/cell death. (*A–C*) MRI showing a left sided intrastriatal graft of killed cells at days 2 (*A*), 7 (*B*), and 35 (*C*) after transplantation. Loss of graft signal and reduction in graft size is noted on the left side, whereas the right side remains unchanged. (*D–F*) Confocal immunofluorescence image (*D*), showing number and morphology of Iba-1-positive cells (green) in close relation to hCNS-SCns (red) in a viable graft. In the dead graft (*E*), morphologically activated Iba-1-positive cells (green) are more abundant and have phagocytosed hCNS-SCns (red) at 35 days after transplantation. (*F*) Iba-1 expression in healthy brain tissue (insert at higher magnification). Nuclei counterstained with DAPI (blue). (*G*) Volumes of dead grafts (filled bar) and viable grafts (open bar) based on MR images at 2, 7, and 35 days after transplantation clearly demonstrates the early volume loss (*, $P < 0.05$). (*H*) quantification of Iba-1-positive cell density surrounding the dying grafts (DG), viable grafts (VG), and in normal parenchyma (NP) at 35 days after transplantation. Results are means ± SEM.

using MRI has been shown, there is a lack of information concerning aspects of stem cell biology including cell proliferation, differentiation, migration, and integration and electrophysiological characteristics. Moreover, most of the studies have used rodent-derived stem cells, and this significantly limits the conclusions that can be made about human cells for use in clinical trials. Here, we prove that the biology of human neural stem cells labeled with SPIO is not altered *in vitro* and *in vivo*, allowing us to monitor the fate of these cells *in vivo* under a variety of transplant conditions over extended periods of time (18 weeks). These findings may have significant impact on the eventual translation of stem cell regenerative medicine to the clinic.

Multipotency is a hallmark of neural stem cells, and we have shown that our hCNS-SCns can differentiate into neurons, astrocytes, and oligodendrocytes (15). Kostura *et al.* raised the concern that cell differentiation could be impaired as they showed that SPIO labeling of mesenchymal stem cells inhibits chondrogenesis but not adipogenesis (12). Here, we found no statistically significant difference in the differentiation potential between SPIO-labeled and unlabeled hCNS-SCns. In addition to cell fate analysis, we bring evidence that magnetic labeling does not affect the electrophysiological characteristics of hCNS-SCns. Resting membrane potentials and classic sodium currents were not different between SPIO-labeled and unlabeled hCNS-SCns. Depolarizing pulses elicited a single action potential. We did not observe spontaneous spiking in either group, which probably reflects the early maturation stage of these cells. Westerlund *et al.* (22) show that neural stem cells *in vitro* go through the same phases as neurons do during development *in vivo*, including up-regulation of inward Na^+ -currents, drop in input resistance, shortening of the action potential, and hyperpolarization of the cell membrane.

MRI of SPIO-Labeled Human Neural Stem Cells. A number of factors affect the MRI detection threshold of SPIO-labeled cells, such as the SPIO concentration per cell, the cell density once the cells integrate into the host, and intrinsic MRI parameters such as field strength, signal to noise ratio (SNR), pulse sequence, and acquisition parameters (23).

Long-term observation of SPIO-labeled stem cells might be limited because of dilution of SPIO with cell division. We found that the relative SPIO concentration was decreased by 50% every 3 days *in vitro*. Nevertheless, it has been shown that cells can be detected for several weeks (10), and we were able to detect clusters of cells by MRI up to 18 weeks. Heyn *et al.* (23) have shown that as little as 1.4–3.0 pg of iron per cell is sufficient for detection with MRI. If we assume an initial content of 20 pg Fe per cell (24) and symmetrical cell division, detection would be possible up to six cell divisions. We know from earlier studies that hCNS-SCns transplanted to the neonatal Nod-Scid brain do continue to proliferate in neurogenic areas of the brain (14). One could hypothesize that cells staying in the SVZ eventually loose their cytoplasmic SPIO. The cells that migrate away early after transplantation and integrate into the host, however, exit the cell cycle and retain the intracellular SPIO over longer time period.

Reports and discussions on MRI cell detection have mainly focused on the minimum number of SPIO-labeled cells detectable with MRI. Although single-cell detection has been reported (25),

most *in vivo* reports have found higher detection limits. We found a detection limit of 1,000 cells *in vitro*, where the cells are highly concentrated (SI Fig. 6*E*). However, once the cells start to migrate and integrate in site-specific manner as observed in the OB and the hippocampus, the density of cells is reduced considerably, leading to a gradual loss of MRI cell signal. Dilution of SPIO during cell division and reduction of cell density during migration and integration are the most important cellular factors determining the detection thresholds of MRI. In contrast to the slow reduction in signal strength found with cell migration, clearance of dead or dying cells as demonstrated in the last experiment (Fig. 4) results in a signal loss in the first 35 days after transplantation. Because dead SPIO-labeled cells result in early loss of MRI signal (Fig. 4) and Iba-1/SC121 double-labeled cells are absent from the main migratory areas, such as the RMS or OB (SI Fig. 8 *G* and *H*), it is unlikely that the observed MRI signal changes are only caused by SPIO laden macrophages.

Early after transplantation, the intracellular SPIO causes a susceptibility artifact most prominent when using gradient echo imaging. Signal changes observed on gradient echo images at this time point significantly overestimated the size of the transplants. Because of this, we found T2-weighted images to be more accurate, especially if volumetric analyses are required. Indeed, quantitative analysis of graft size on T2-weighted images was comparable with measurements on histological sections (SI Fig. 6). At later time points however, when cell density decreases as cells integrate, gradient echo imaging proved to be more reliable for cell detection than T2-weighted spin echo imaging.

The Migration Pattern of hCNS-SCns Depends on the Microenvironment. Whereas hCNS-SCns migrated along the RMS and the corpus callosum and integrated into the OB and the hippocampus in the uninjured immature brain, an injury was required in the adult brain to initiate stem cell migration. *In vivo* stem cell tracking, using MRI, allowed this process to be followed longitudinally.

In a previous study (14), we demonstrated widespread migration of human cells when transplanted into the neonatal brain. The extent and pattern of hCNS-SCns migration transplanted to the neonatal brain are similar to those found for endogenous stem cells (26), which migrate from the SVZ to the OB where they differentiate into local interneurons (27). MRI showed that hCNS-SCns migrate along the RMS leading them into the core of the OB at a very early time point after transplantation. This may be due to directed currents of CSF generated by ciliary beating of ependymal cells leading to rapid distribution of transplanted hCNS-SCns (32). This early migration pattern was followed by a radial migration where hCNS-SCns adopted a laminar organization in the granular and periglomerular layers of the OB. It was striking that in the olfactory bulb and the hippocampus the human cells displayed remarkable regional specificity and also adopted cell body diameters of the local host cells as described in ref. 17.

In contrast to the immature brain, transplanted hCNS-SCns did not show spontaneous migration in the uninjured adult brain. However, if an injury occurs, transplanted hCNS-SCns undergo targeted migration toward stroke (as described in ref. 6). Stem cells have been shown to cross from the contralateral hemisphere via a transcallosal path toward the lesion site (10). We describe long-term sequential *in vivo* MR imaging of ipsilateral transcortical-targeted migration of human stem cells with correlative histology. In contrast to long distance transcallosal migration described by others (9, 20), we found that the extent of transcortical migration was determined by the distance between the graft site and the lesion. If the distance between the lesion and the graft site in the rat brain exceeded 1 mm, we did not find targeted migration. This contrasts with reports where long range migration of stem cells in the stroked brain was observed (10, 11). These other studies, however, were done by using rodent-derived stem cells. There are fundamental differences between cells lines used in our and others' studies, such as migratory behavior, the degree of maturation, and the species from which the cells are derived. Hence, comparison between individual studies is very difficult. This finding emphasizes the need to control for post transplantation graft location in relation to an evolving lesion.

Analysis of migration and cell fate revealed equivalent biological properties of SPIO-labeled and unlabeled hCNS-SCns. It has been speculated that release of iron oxide particles from dying cells into the host parenchyma could lead to a prolonged inflammatory response after transplantation. We did not find a difference in Iba-1 expression between animals receiving SPIO-labeled hCNS-SCns as compared with nonlabeled cells.

Conclusion

In this report we provide an in-depth analysis of human neural stem cell biology after magnetic labeling and transplant to the rodent brain. We have shown that human neural stem cells labeled with SPIO survive in large numbers, are able to differentiate into neuronal and glial lineages, have neuronal-like electrophysiological characteristics, and appropriately respond to microenvironmental cues after transplantation to the rodent brain. Using MRI and histology, we show that upon transplantation into the immature rodent brain, SPIO-labeled hCNS-SCns migrate and integrate in a manner appropriate for their location. Conversely, in the mature brain, targeted migration is observed only when an injury occurs. Using a cortical stroke model, we demonstrate that MRI is able to depict transcallosal and transparenchymal-targeted migration. And finally, we demonstrate that death of transplanted cells can be monitored by using *in vivo* MRI.

Neurotransplantation holds great promise for the treatment of acute and chronic central nervous system disease. *In vivo* cellular imaging will eventually serve multiple purposes, including postoperative visualization of graft location, tracking cell migration and integration, and monitoring graft survival.

Methods

Human CNS Stem Cells Derived Neurosphere Cells. hCNS-SCns (StemCells, Inc., Palo Alto, CA) were isolated by flow cytometry from fetal brain tissue (16–20 wk) as described in refs. 13 and 14. hCNS-SCns cells were plated at 10^5 cells per ml in human neurosphere culture media (X-VIVO 15 medium; BioWhittaker, Walkersville, MD), N-2 supplement (GIBCO, Carlsbad, CA), and 0.2 mg/ml heparin supplemented with basic fibroblast growth factor (20 ng/ml), EGF (20 ng/ml), and leukemia inhibitory factor (10 ng/ml). On the day of transplantation, cells were prepared at a density of 1×10^5 cells per μl.

Magnetic Labeling of Neural Stem Cells. SPIO particles (Feridex IV; Berlex Laboratories, Wayne, NJ) and protamine sulfate (American Pharmaceuticals Partner, Schaumburg, IL) (5 μg/2.5 μg/ml) were incubated for 30min at 37° in culture medium before being added to the cells for 24 h (SI Fig. 11). For relative measurement of cellular SPIO, content hCNS-SCns were fixed after 1, 3, 6, and 9 days *in vitro* and stained with an anti-dextran antibody (DX-1, StemCell Technologies, Vancouver, BC), and the staining per cell was determined by using a particle analyzer function (ImageJ software). For cell differentiation assay, SPIO-labeled and unlabeled cells were grown in *ex vivo* base without mitogens and supplemented with BDNF, GDNF, and laminin for 10 days. Immunofluorescence staining for Nestin, β-tubulin, and GFAP was done, and the percent of immunoreactive cells was counted.

Whole-Cell Patch Clamp Experiments. Whole-cell recordings were made essentially as described in ref. 28. Morphologically, neuronal appearing cells (phase-bright somata with two to five primary processes) present in each condition (SPIO-labeled and unlabeled hCNS-SCns) were selected for recording ($n = 6$ for each condition). For evoking sodium currents, cells were held at -70 mV in voltage

clamp and subjected to depolarizing step functions. For evoking, action potentials cells were maintained at −70mV in current clamp and stimulated with a depolarizing current injection.

MRI. High-resolution magnetic resonance images were acquired on a 4.7T/40 cm animal scanner system (Varian, Palo Alto, CA). The imaging protocol consisted of scout imaging in two planes followed by a spin-echo sequence (TR = 2500 msec, TE = 45 msec, NEX = 4, matrix = 256 × 256, FOV = 40 mm, slice thickness = 1 mm, gap = 0 mm) and a 3D gradient echo scan (TR/TE1 = 600 ms/5 ms, NEX = 4, matrix 128 × 128 × 64, FOV 3 × 3 × 3 cm resulting in a voxel size of 234 × 234 × 469 μm). For *in vitro* studies cells were injected into agarose gel phantoms. During imaging animals were under isoflurane anesthesia and monitored for respiration and heart rate, the temperature was kept at 37°C, using a feedback controlled system.

Cell Transplantation in Neonatal NOD-SCID Mice. All animal procedures were approved by the Stanford University Administrative Panel on Laboratory Animal Care. Neonatal mice (postnatal day 0–postnatal day 1) were cryoanesthetized by placing them in ice for 5–10 min followed by stereotactic injection of either SPIO-labeled ($n = 16$) or unlabeled hCNS-SCns ($n = 12$) into the lateral ventricle (2 μl of cells at 1×10^5 cells per μl). MRI was performed at 3, 9, 12, and 18 weeks after transplantation. Engraftment of human cells was tested histologically for each time point.

Distal Middle Cerebral Artery Occlusion (dMCAo). Adult male Sprague–Dawley rats ($n = 10$) were anesthetized with isoflurane and the left common carotid artery temporarily occluded for 1 h. The distal middle cerebral artery was exposed, cauterized, and cut just above the rhinal fissure.

Cell transplantation in rat after dMCAO. Seven days after dMCAO, rats were given 1.0-μl deposits of suspended cells (1×10^5 cells per μl), using a micropump in three cortical regions in the anterior-posterior axis (SI Fig. 12). Rats were immunosuppressed by daily i.p. injection of cyclosporine A (10 mg/kg). Five weeks posttransplantation, rats were transcardially perfused with 4% phosphate-buffered paraformaldehyde and processed for histology.

Histology and Immunohistochemistry. For Prussian blue staining, mounted sections were washed and incubated for 20 min in 10% potassium ferrocyanide and 20% hydrochloric acid. Triple-label immunofluorescence staining was carried out on free-floating sections. Sections were incubated overnight at 4°C with either the human-specific nuclear (SC101, 1:1,000) or cytoplasmic marker (SC121 1:3,000, both provided by StemCells, Inc.) and one of the following makers: rabbit anti-β-tubulin III (Tuj-1, 1:2,000; Covance Research Products, Berkeley, CA), guinea-pig anti-GFAP (1:500; Advanced ImmunoChemicals, Long Beach, CA), goat anti-doublecortin (Dcx, 1:100; Santa Cruz Biotechnology, Santa Cruz, CA), human-specific mouse anti-GFAP (1:3,000; provided by StemCells Inc.), mouse anti-MAP2 (1:3,000, Abcam, Cambridge, MA), rat anti-Iba-1 (ionized calcium binding adapter molecule 1, 1:2,000; Wako Bioproducts, Richmond, VA). Secondary antibodies used were Alexa Fluor 488 and 546, (1:1,000; Molecular Probes, Eugene, OR) or Cy3 (1:2,000; Jackson ImmunoResearch Laboratories, West Grove, PA). DAPI (1:1,000; Sigma–Aldrich, St. Louis, MO) was used to label nuclei. For total counting of SC101-positive cells, a biotinylated anti-mouse secondary antibody (1:250; Vector Laboratories, Burlingame, CA), followed by streptavidin-HRP and DAB enhancement were used.

Microscopical Analysis. Total numbers of transplanted human cells stained with SC101 were counted by using unbiased computational stereology (Stereoinvestigator software, MicroBrightfield, Brattleboro, VT). For cell fate analysis, the proportion of SC101-labeled cells that also stained with lineage-specific phenotype markers was determined by confocal microscopy. Split-panel and *z* axis analyses were used for all counting. Fifty or more SC101-positive cells were scored for β-tubulin and GFAP in each anatomical area (SVZ, RMS, and OB) per animal.

Statistics. The statistic software package PRISM (GraphPad, San Diego, CA) was used for data analysis. All means are presented ± SEM. Statistical differences were assessed either by a nonparametric Mann–Whitney *U* test or by a one-way Kruskal–Wallis test. The level of significance was set at $P < 0.05$.

We thank Dr. Bruce Schaar for critical reading of the manuscript and Beth Hoyte for preparation of the figures. This work was funded by United States National Institutes of Health National Institute of Neurological Disorders and Stroke Grants 2R01 NS27292 and 2P01 NS37520, Russell and Elizabeth Siegelman, the William Randolph Hearst Foundation, Bernard and Ronni Lacroute (to G.K.S.), and Swiss National Science Foundation Grants PBBEB-104450 and SSMBS-1194/PASMA-108940/1 (R.G.).

1. Mendez I, Sanchez-Pernaute R, Cooper O, Viñuela A, Ferrari D, Björklund L, Dagher A, Isacson O (2005) *Brain* 128:1498–1510.
2. Lindvall O, Brundin P, Widner H, Rehncrona S, Gustavii B, Frackowiak R, Leenders KL, Sawle G, Rothwell JC, Marsden CD (1990) *Science* 247:574–577.
3. Olanow CW, Goetz CG, Kordower JH, Stoessl AJ, Sossi V, Brin MF, Shannon KM, Nauert GM, Perl DP, Godbold J, Freeman TB (2003) *Ann Neurol* 54:403–414.
4. Freeman TB, Cicchetti F, Hauser RA, Deacon TW, Li XJ, Hersch SM, Nauert GM, Sanberg PR, Kordower JH, Saporta S, Isacson O (2000) *Proc Natl Acad Sci USA* 97:13877–13882.
5. Kondziolka D, Steinberg GK, Wechsler L, Meltzer CC, Elder E, Gebel J, Decesare S, Jovin T, Zafonte R, Lebowitz J *et al.* (2005) *J Neurosurg* 103:38–45.
6. Kelly S, Bliss TM, Shah AK, Sun GH, Ma M, Foo WC, Masel J, Yenari MA, Weissman IL, Uchida N *et al.* (2004) *Proc Natl Acad Sci USA* 101:11839–11844.
7. Modo M, Stroemer RP, Tang E, Patel S, Hodges H (2002) *Stroke* 33:2270–2278.
8. Norman AB, Thomas SR, Pratt RG, Lu SY, Norgren RB (1992) *Brain Res* 594:279–283.
9. Hawrylak N, Ghosh P, Broadus J, Schlueter C, Greenough WT, Lauterbur PC (1993) *Exp Neurol* 121:181–192.
10. Hoehn M, Kustermann E, Blunk J, Wiedermann D, Trapp T, Wecker S, Focking M, Arnold H, Hescheler J, Fleischmann BK, *et al.* (2002) *PNAS* 99:16267–16272.
11. Modo M, Mellodew K, Cash D, Fraser SE, Meade TJ, Price J, Williams SCR (2004) *NeuroImage* 21:311–317.
12. Kostura L, Kraitchman DL, Mackay AM, Pittenger MF, Bulte JW (2004) *NMR Biomed* 17:513–517.
13. Tamaki S, Eckert K, He D, Sutton R, Doshe M, Jain G, Tushinski R, Reitsma M, Harris B, Tsukamoto A, *et al.* (2002) *J Neurosci Res* 69:976–986.
14. Uchida N, Buck DW, He D, Reitsma MJ, Masek M, Phan TV, Tsukamoto AS, Gage FH, Weissman IL (2000) *Proc Natl Acad Sci USA* 97:14720–14725.
15. Cummings BJ, Uchida N, Tamaki SJ, Salazar DL, Hooshmand M, Summers R, Gage FH, Anderson AJ (2005) *Proc Natl Acad Sci USA* 102:14069–14074.
16. Claiborne BJ, Amaral DG, Cowan WM (1990) *J Comp Neurol* 302:206–219.
17. Muotri AR, Nakashima K, Toni N, Sandler VM, Gage FH (2005) *Proc Natl Acad Sci USA* 102:18644–18648.
18. Modo M, Hoehn M, Bulte JW (2005) *Mol Imaging* 4:143–164.
19. Bulte JW, Zhang S, van Gelderen P, Herynek V, Jordan EK, Duncan ID, Frank JA (1999) *Proc Natl Acad Sci USA* 96:15256–15261.
20. Lee IH, Bulte JW, Schweinhardt P, Douglas T, Trifunovski A, Hofstetter C, Olson L, Spenger C (2004) *Exp Neurol* 187:509–516.
21. Modo M, Cash D, Mellodew K, Williams SCR, Fraser SE, Meade TJ, Price J, Hodges H (2002) *NeuroImage* 17:803–811.
22. Westerlund U, Moe MC, Varghese M, Berg-Johnsen J, Ohlsson M, Langmoen IA, Svensson M (2003) *Exp Cell Res* 289:378–383.
23. Heyn C, Bowen CV, Rutt BK, Foster PJ (2005) *Magn Reson Med* 53:312–320.
24. Frank JA, Miller BR, Arbab AS, Zywicke HA, Jordan EK, Lewis BK, Bryant LH, Jr, Bulte JW (2003) *Radiology* 228:480–487.
25. Shapiro EM, Skrtic S, Sharer K, Hill JM, Dunbar CE, Koretsky AP (2004) *Proc Natl Acad Sci USA* 101:10901–10906.
26. Suhonen JO, Peterson DA, Ray J, Gage FH (1996) *Nature* 383:624–627.
27. Lois C, Alvarez-Buylla A (1994) *Science* 264(5162):1145–1148.
28. Stellwagen D, Beattie EC, Seo JY, Malenka RC (2005) *J Neurosci* 25:3219–3228.